ADVANCED MATERIALS
www.advmat.de

Soft Multimaterial Magnetic Fibers and Textiles

*Hritwick Banerjee, Andreas Leber, Stella Laperrousaz, Rémi La Polla, Chaoqun Dong, Syrine Mansour, Xue Wan, and Fabien Sorin**

Magnetically responsive soft materials are promising building blocks for the next generation of soft robotics, prosthesis, surgical tools, and smart textiles. To date, however, the fabrication of highly integrated magnetic fibers with extreme aspect ratios, that can be used as steerable catheters, endoscopes, or within functional textiles remains challenging. Here, multimaterial thermal drawing is proposed as a material and processing platform to realize 10s of meters long soft, ultrastretchable, yet highly resilient magnetic fibers. Fibers with a diameter as low as 300 µm and an aspect ratio of 10^5 are demonstrated, integrating nanocomposite domains with ferromagnetic microparticles embedded in a soft elastomeric matrix. With the proper choice of filler content that must strike the right balance between magnetization density and mechanical stiffness, fibers withstanding strains of >1000% are shown, which can be magnetically actuated and lift up to 370 times their own weight. Magnetic fibers can also integrate other functionalities like microfluidic channels, and be weaved into conventional textiles. It is shown that the novel magnetic textiles can be washed and sustain extreme mechanical constraints, as well as be folded into arbitrary shapes when magnetically actuated, paving the way toward novel intriguing opportunities in medical textiles and soft magnetic systems.

1. Introduction

Stimuli-responsive, untethered soft actuators are becoming key components in wearable electronics, human-machine interaction, bioengineering, health care, and smart textiles.[1–6] Numerous possible actuation mechanisms exist based on temperature,[7–9] light,[10,11] acoustic,[12,13] chemical reaction,[14,15] and magnetic[16–18] activation—each with their strengths and weaknesses.[19–21] Among these various strategies, magnetic actuators stand out in several avenues, including output energy density, remote excitation, device footprint, and achievable actuation force.[22–24] As a result, the exploitation of soft magnetic actuators is increasingly investigated in a variety of configurations including micro/nanorobots,[25–27] morphing architectures,[28,29] bioinspired robots,[30,31] and catheters.[18,32] Of particular interest are magnetic systems with fiber-like high aspect ratio architectures, that are very well suited for minimally invasive surgical and diagnosis tools, remote monitoring along large structures, or for integration within smart textiles.[33–35]

To fabricate magnetically responsive soft materials and systems, 3D printing,[16,36] molding and casting,[18,37,38] and lithography[39–42] techniques are commonly employed. Though these processes work very well for small-scale systems and low aspect ratio devices, they are as well adapted for configurations where longer lengths of fibers are required, as is the case for fabrics and wearables, soft robotics, and human–robot interfaces. Particle flow spinning has also been used to fabricate stretchable magnetic yarns for self-powered mechanical sensing[43] and magnetoelectrical clothing generator.[44] However, the ability to integrate several functionalities that can complement a magnetic actuation mechanism remains very challenging despite high interest and extended research efforts.[45–47] Combining actuation with sensing, the delivery of optical and electrical signals, or microfluidics capabilities, would constitute a significant breakthrough in applications such as smart catheters and soft medical textiles.[48]

Recent advances in multimaterial fiber processing techniques have been paving the way toward the integration of several advanced functionalities in a single fiber, as well as within textiles.[49–52] A first important breakthrough was the ability to co-draw metals, insulators, and semiconductors in a single fiber, establishing the thermally drawn multimaterial fiber concept.[53–55] Subsequently, it was demonstrated that this fiber-processing approach could also be applied to claddings beyond glasses and rigid thermoplastics, namely materials such as biodegradable[56] and food-grade polymers,[52] or soft thermoplastic elastomers (TPEs).[57] Combined with the processing of polymer nanocomposites, liquid metals, and the ability to maintain architectures with small feature sizes, novel fiber devices could be demonstrated for sensing,[58,59] energy harvesting,[49,60] and even tendon-based multimaterials soft catheters.[48] Thus far, however,

H. Banerjee, A. Leber, S. Laperrousaz, R. La Polla, C. Dong, S. Mansour, X. Wan, F. Sorin
Institute of Materials
École Polytechnique Fédérale de Lausanne
1015 Lausanne, Switzerland
E-mail: fabien.sorin@epfl.ch

The ORCID identification number(s) for the author(s) of this article can be found under https://doi.org/10.1002/adma.202212202

DOI: 10.1002/adma.202212202

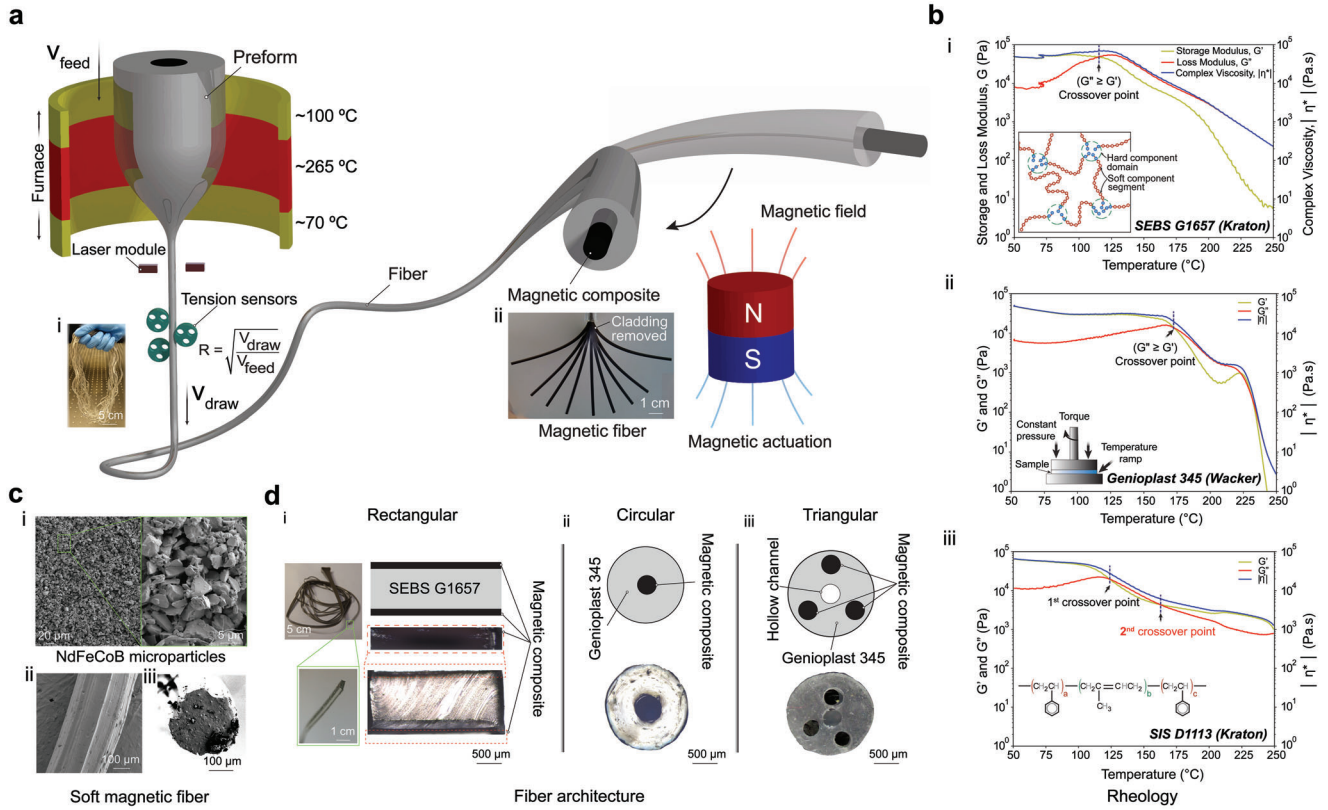

Figure 1. Magnetic multimaterial fiber manufacturing, rheology, and structure. a) Schematic of the thermal drawing fabrication technique and the magnetic tether-free actuation. The inset depicts a photograph of a 20 m-long continuous fiber (i) and magnetic fiber actuation (ii). b) Oscillatory shear rheology analysis under increasing temperature for SEBS G1657 (Kraton) (i), Genioplast 345 (Wacker) (ii), and SIS D1113 (Kraton) (iii). c) Scanning electron microscopy (SEM) image for NdFeCoB ferromagnetic microparticles, magnetic fibers (i) with cladding removed (top) (ii), and cross-sectional view (iii). d) Optical microscopy images of magnetic fiber's different architecture: i) rectangular, ii) circular, and iii) triangular.

magnetic properties have seldom been investigated within the realm of fiber devices and advanced fabrics. In particular, thermal drawing has not been applied to magnetic materials, and the ability to make fibers and textiles with advanced sensing and delivery capabilities, combined with magnetic attributes, remains challenging.

Here, we propose a novel materials and processing platform to realize highly integrated soft magnetic fibers and textiles. Our strategy relies on the thermal drawing of magnetic composites where we could identify, via an in-depth rheological, thermomechanical, and computed tomography analysis, the right combination of magnetic filler and elastomeric matrix. We demonstrate thermally drawn magnetic fibers with diameters as small as 300 µm and aspect ratios of 10^5 that can integrate several magnetic domains in prescribed positions, enabling intricate 3D motion profiles. Via a careful analysis of the effect of the ferromagnetic filler on the mechanical and magnetic properties, we could identify the optimal weight percentage filler to realize large magnetic actuation and demonstrate fibers that can lift up to 370 times their own weight. Exploiting the ability to magnetize selectively different areas along the fiber axis, we demonstrate thermally drawn magnetic fibers with complex modes of deformation and tortuous path navigation. Leveraging the versatility of the multimaterial fiber platform, we could also realize magnetic fibers with embedded microchannels for targeted drug delivery applications. Finally, we exploit this novel platform in the context of medical textiles, by weaving soft magnetic fibers into textiles programmed with specific magnetization orientations along the fiber axis to realize complex shape morphing. We demonstrate a fabric capable of applying a force of 22 N, which could pave the way toward intriguing breakthroughs for rehabilitation medical textiles.

2. Results and Discussion

The fabrication and actuation concepts are represented schematically in **Figure 1**a. The thermal drawing process consists in first assembling different materials in a prescribed architecture within a macroscopic object conventionally called a preform. The structure is then heated above the softening points of the constituents and thermally pulled to form an elongated fiber. While the cross-sectional structure is preserved from preform to fiber, the feature sizes scale-down by a factor called the draw-down ratio (R), and the length increases by a factor of R^2 from volume conservation (Figure 1a(i,ii)). For multimaterial co-drawing to be successful, the constituents must exhibit compatible thermomechanical and rheological properties.[57] Particularly when the desired feature sizes at the fiber level must be small (typically the order of a few micrometers to a few nanometers), it is key to process materials at high viscosities (higher than 10^3 Pa s).[50,51,53,61]

Physically crosslinked copolymers constitute an intriguing class of materials to realize soft and stretchable fiber-based devices.[49,52,57] Similarly to their thermoplastic counterparts, above their glass transition temperature (T_g), these materials undergo a transition from a rigid state to a flexible and rubbery state, where the loss modulus (G'') dominates over the storage modulus (G'). In such a temperature window, the TPEs can be deformed into a fiber, while they recover the hard and soft domain's configuration when cooling down to room temperature (Figure 1b(i) inset).[62] This trend is observed for several TPEs such as poly(styrene-*b*-(ethylene-*co*-butylene)-*b*-styrene) (SEBS) G1657 (Kraton) with a high molecular weight (70 kg mol^{-1}), Genioplast 345 (Wacker), and styrene-isoprene-styrene (SIS) D1113 (Kraton) as shown in Figure 1b(i-iii). Due to their polystyrene-based nature, SEBS G1657 and SIS D1113, crossover ($G'' \geq G'$) happened at ≈115 and ≈124 °C, respectively (Figure 1b(i,iii)), while Genioplast 345, a silicone-based copolymer that contains > 90% siloxane, exhibits a crossover at a higher temperature of ≈173 °C (Figure 1b(ii)). Beyond the crossover temperature, the viscosity steadily decreases for all materials but is dominated by a viscous response. Note that SIS D1113 experiences a second crossover of G' and G'' at ≈162 °C. Its double bond (see Figure 1b(iii) inset) is prone to interact with the surrounding medium, limiting the resistance to oxidation and accelerating thermal degradation. For simplicity, we will refer to SEBS G1657, Genioplast 345, and SIS D1113 as SEBS, Genioplast, and SIS, respectively, throughout the manuscript.

To impart thermally drawn fibers with magnetic properties, together with the mechanical attributes of elastomers, we designed and fabricated magnetic TPE microcomposites. Composites can combine the rheological properties of the matrix required for thermal drawing, while exhibiting magnetic properties inherited from the ferromagnetic microparticle fillers. The choice for the ferromagnetic material takes into account the need for residual magnetization coupled with a high coercivity so that it can maintain its magnetic properties for actuation, which favors hard-ferromagnetic materials. Due to their higher coercivity, maximum energy density product $(\mathbf{BH})_{max}$ (where **H** is the externally applied magnetic field and **B** the magnetic induction), and high Curie temperature of 360 °C, we select neodymium–iron–cobalt–boron (NdFeCoB) alloy-based microparticles of diameter ≈2–5 µm as magnetic fillers (Figure 1c(i)). For the soft matrix that will encapsulate the hard particles, physically cross-linked elastomers are favored as presented above. One key aspect of the thermal drawing process is that complex multimaterial structures can be realized, with diameters as low as 300 µm, over 10s of meters of fiber length (Figure 1c(ii,iii)). We demonstrate this design freedom by fabricating several magnetic fiber architectures with different cross-sectional geometries, and with several magnetic composite domains positioned in various patterns within a TPE cladding (Figure 1d(i–iii)).

To find the best material host for the ferromagnetic particles among various TPEs, we investigate microcomposites formed with the three TPEs presented above. 10–25 vol% NdFeCoB-SEBS composites (that is referred to as magnetorheological elastomers (MREs); MRE 10, SEBS-MRE 25, SEBS) demonstrate a similar rheological behavior to SEBS as can be seen in **Figure 2**a and Figure S1 (Supporting Information). MRE 30, SEBS on the other hand, as well as composites with volume fraction higher than 25%, exhibit no crossover point during the temperature ramp (Figure S1, Supporting Information), which makes them not well suited for the thermal drawing process. Higher filler content indeed can result in a particle network between the polymer chains that hinder their long-range motion. This phenomenon can be explored in a rheological experiment with a stress amplitude sweep, as shown in Figure 2b. This trend favors shear-thinning behavior and led the composite to act as a thixotropic paste (Figures S2 and S3, Supporting Information).

To explore magnetic composites with different matrix materials, we compare MRE 20, SEBS with Genioplast and SIS counterparts. Figure S1 (Supporting Information) shows that MRE 20, SEBS and MRE 20, Genioplast have a crossover point at 115 and 178 °C respectively, while, MRE 20, SIS does not exhibit such a signature, making it more difficult to be thermally drawn. At the crossover point (see Figure S4, Supporting Information), the critical complex viscosity values ($|\eta_c^*|$) for MRE 20, SEBS and MRE 20, Genioplast are ≈2×10^5, 5×10^4 Pa s, respectively. A higher viscosity can help in the design of more complex architectures[61] and hence NdFeCoB, SEBS composites are favored in the remainder of this study.

To understand the effect of thermal drawing on the distribution of magnetic particles, and in particular, the formation of aggregates, percolation paths, or preferential orientation which could all influence the magnetic properties, we turn to X-ray computed tomography analysis. We investigated both preforms and fibers that were segmented to form 2D microscopy images and then reconstructed computationally into 3D images (see Figure S5, Supporting Information). A histogram with barycenter distribution is overlaid through the image slices from surface-to-core-to-surface of the magnetic composites (see Figure S6, Supporting Information). We perform computational reconstruction with Gaussian distribution that presented a barycenter variance of 0.613 at the preform level, reduced to 0.163 at the fiber level, a multifold improvement that highlights the positive effect of thermal drawing on the particle distribution at the fiber level (Figure 2c). We observe a similar trend with the formation of aggregates skewness profile going from 0.865 at the preforms level, to 0.027 for fibers, >30 times improvement in magnetic particles' distribution within the MRE 20, SEBS matrix. The induced alignment observed leads to percolation paths during thermal drawing (Figure 2d), and a homogeneous distribution of the particles that favor a good response to magnetic field as we investigate below.

We now turn to the magnetic characterization of thermally drawn composites via a four-quadrant magnetic hysteresis measurement as shown in Figure 2e. The measurement reveals a residual magnetism (M_r) of ≈36.25, 50.1, 61.25, and 85 A m^2 kg^{-1} for MRE 10, SEBS, MRE 15, SEBS, MRE 20, SEBS, and MRE 25, SEBS, respectively. These values are on par with state-of-the-art values found for magnetic composites,[18] and allow for a variety of magnetic actuation configurations as we will show below. As expected, the magnetization increases as the volume fraction of the magnetic particle is larger, yet the coercive field (H_c) that is an intrinsic material property remains unchanged at ≈1 T. Note that it is possible to magnetize along various directions different fiber domains along the axis, which will be exploited below to generate different actuation movements from fibers and textiles.

Next, we address the mechanical properties of the fabricated magnetic fibers via tensile testing. We focus on thermally drawn

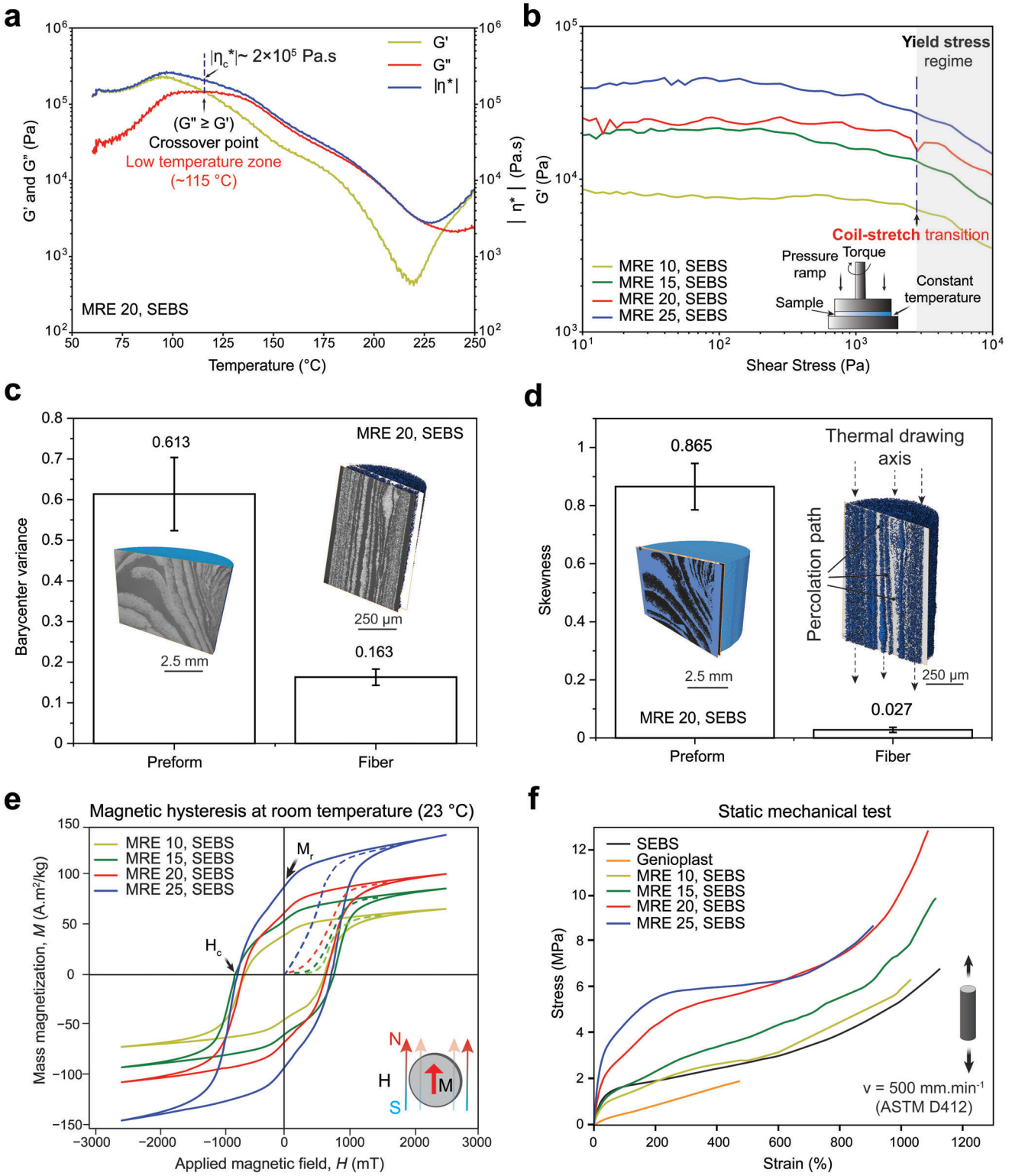

Figure 2. Rheology, X-ray computed tomography, magnetic, and mechanical characterization. a) Oscillatory shear rheology under increasing temperature for MRE 20, SEBS. b) Storage modulus as a function of the oscillation stress amplitude at 160 °C with stress amplitude sweep. c,d) X-ray computed tomography photographs and analysis for magnetic composites at the preform and the thermally drawn fiber stage. e) Magnetization curves with magnetic hysteresis loops of composite magnetic materials at room temperature. f) Static tension test for TPEs and magnetic fiber samples at an extension rate of 500 mm min^{-1}.

fibers which are composed of 10–25 vol% NdFeCoB-SEBS as the fiber core. We remove the Genioplast cladding layer to investigate the mechanical properties of the composites alone. As elastomers exhibit non-linear stress–strain curves, the modulus is expressed by the stress value at 100% strain. At a strain rate of 500 mm min^{-1} following the ASTM D412 standard, the MRE 10, MRE 15, MRE 20, and MRE 25 composites exhibit a modulus at 100% strain of 1.7, 1.81, 3.1, and 4.43 MPa, respectively (Figure 2f). In comparison, pure Genioplast fibers are particularly soft, with a 100%-modulus of 0.54 MPa, while SEBS is a relatively stiffer material with a 100%-modulus of 1.54 MPa (Figure 2f). Interestingly also, all TPEs employed in this work exhibit high elongations at break, outperforming the commonly used elastomer for soft and stretchable devices poly(dimethylsiloxane) (PDMS, Sylgard-184) with an elongation at break typically of 100%.[63] The lowest value of 470% is found for Genioplast fiber, while SEBS fiber is found to break at 1123%. Elongation at the break for MRE 10, MRE 15, MRE 20, and MRE 25 magnetic fibers are exhibited as 1002%, 1113%, 1086%, and 905%, respectively (Figure 2f). The uniform distribution of the magnetic microparticles coupled with their increased axial orientation after thermal drawing induces an effective stress transfer during uniaxial stretching, which contributes to increasing the elastic modulus and the tensile strength.[64] Owing to the viscoelastic nature of the MREs, SEBS, and Genioplast, a decrease in strain rate from 500 to 50 mm min^{-1} leads to the activation of particular molecular mobility, often due to side-chain motion or ring flips called the β-transition.[65] This phenomenon thus leads to a lower Young's modulus and an increase of elongation at break for MREs, SEBS, and Genioplast fibers as depicted in Figure S7, (Supporting Information).

We also tested the mechanical properties of soft and magnetic fibers against dynamic strain-stress measurements, where the fiber samples are repeatedly stretched between 0% and 100% for 10 cycles with an extension speed of 50 mm min^{-1} (Figure S8, Supporting Information). All investigated TPEs and composites exhibited a hysteresis behavior where the unloading curve deviates from the loading curve. A remanent deformation, also termed "tensile set", is observed, which is quantified by the strain at which the unloading curve crosses the 0-stress horizontal line. The remanent deformation is the result of viscous and plastic contributions to the dominantly elastic deformation.[66]

We now turn to the response of thermally drawn soft magnetic fibers to an external magnetic field and the ability to actuate mechanical movement (**Figure 3**a,b). After thermal drawing, the multimaterial fibers are magnetized under a magnetic field of ≈2.4 T (Figure 3a,b(i)), as we discussed earlier and as detailed in the experimental section. Once magnetized, we bring near the fiber a cylindrical permanent magnet that generates an external magnetic field of ≈120 mT, and investigate the bending and force applied by the fiber onto a load cell (Figure 3a,b(iii)). The intensity of the magnetic field is inversely proportional to the distance squared between the magnet and the fiber,[67] as also seen experimentally in Figure S9, (Supporting Information). To account for the influence of peripheral devices such as the microcontroller and electrical cables, we perform experiments without the magnetic fibers first, which generated a force of ≈5.5 mN as presented in Figure S10, (Supporting Information). This stray magnetic field effect is deducted computationally from all subsequent experiments performed on magnetic fibers. For the experiments, we chose 6 cm long fibers with a 300 µm diameter, and could measure a maximum force of 47 mN for fibers magnetized perpendicularly to their axis, while sagittal-plane magnetization along the fiber axis resulted in a maximum force of 36 mN as depicted in Figure 3a(ii,iii) and Figure 3b(ii,iii), respectively.

Next, we evaluate the lifting force that could be generated by a soft magnetic fiber. We attached a 9 cm long and 300 µm diameter fiber to a 25 cm long model skeletal leg (Figure 3c(i)). The cylindrical permanent magnet was moved vertically producing a nonuniform magnetic field of ≈140 mT to flex the skeletal leg (Figure 3c(ii)). Repetitive cycles with different magnet velocities induced repeatedly the flection of the skeletal leg (Figure 3c(iii,iv)). 3D printed rings were stacked onto the model skeletal ankle and the magnetic fiber was able to lift a weight of 39.10 g, which represents ≈370 times the fiber weight (Figure 3c(v); Movie S1, Supporting Information). We demonstrate a similar proof-of-concept study with a skeletal arm that bears weight, for flection and extension in a repetitive manner, indicating magnetic fiber's resiliency (Figure S11 and Movie S2, Supporting Information). These results confirm the ability to steer thermally drawn magnetic composites, and apply a force when magnetically actuated.

To highlight the potential of our new materials and processing platform, we first investigate the use of a single magnetic fiber as an advanced minimally invasive surgical tool that can be magnetically guided to navigate within a human stomach phantom model (Figure 3d–f). Thanks to the flexibility of the multimaterial thermal drawing process, we can fabricate fibers with complex architectures and in particular several magnetic cores organized in various configurations. For example, we realized, in a single and continuous drawing step, a fiber integrating 3 magnetic composite domains positioned at 120° to one another as shown in Figure 3d(i,ii). As an additional capability, we designed a hollow channel at the center of the fiber for, for example, drug delivery applications. We employed Genioplast as an encapsulating matrix owing to its low elastic modulus thus entailing a small magnitude of the magnetic field to generate multidirectional deformation and twist the fibers for tortuous path navigation. We used an aspect ratio (ratio of length to diameter) of the magnetic fibers of 260, but aspect ratios as high as 1050 were also achieved. An external magnetic field of 280 mT was applied to steer the magnetic fiber in the desired direction within the human stomach phantom and carry out a set of tasks, as shown in Figure 3e,f. In the first step, the fiber navigates within the tortuous path and conforms to the curvature of the model. Next, the magnetic fiber-based model catheter is maneuvered toward a simulated diseased tissue and a fluid is injected through the center hollow channel and delivered precisely to the desired location, showcasing the targeted drug delivery functionality. Finally, the magnetic fiber was retracted using the same external magnetic field configuration (Movie S3, Supporting Information).

To establish that the magnetic fiber can safely deliver drugs without degradation, we use a 20-cm long fiber and flew a CD-C11-6'SLN drug solution for H1N1 virus treatment inside one of its hollow channels. We tested the model drug activity by infecting Madin-Darby canine kidney (MDCK) cells with the H1N1 virus. Figure 3g demonstrates that the percentage of infected cells

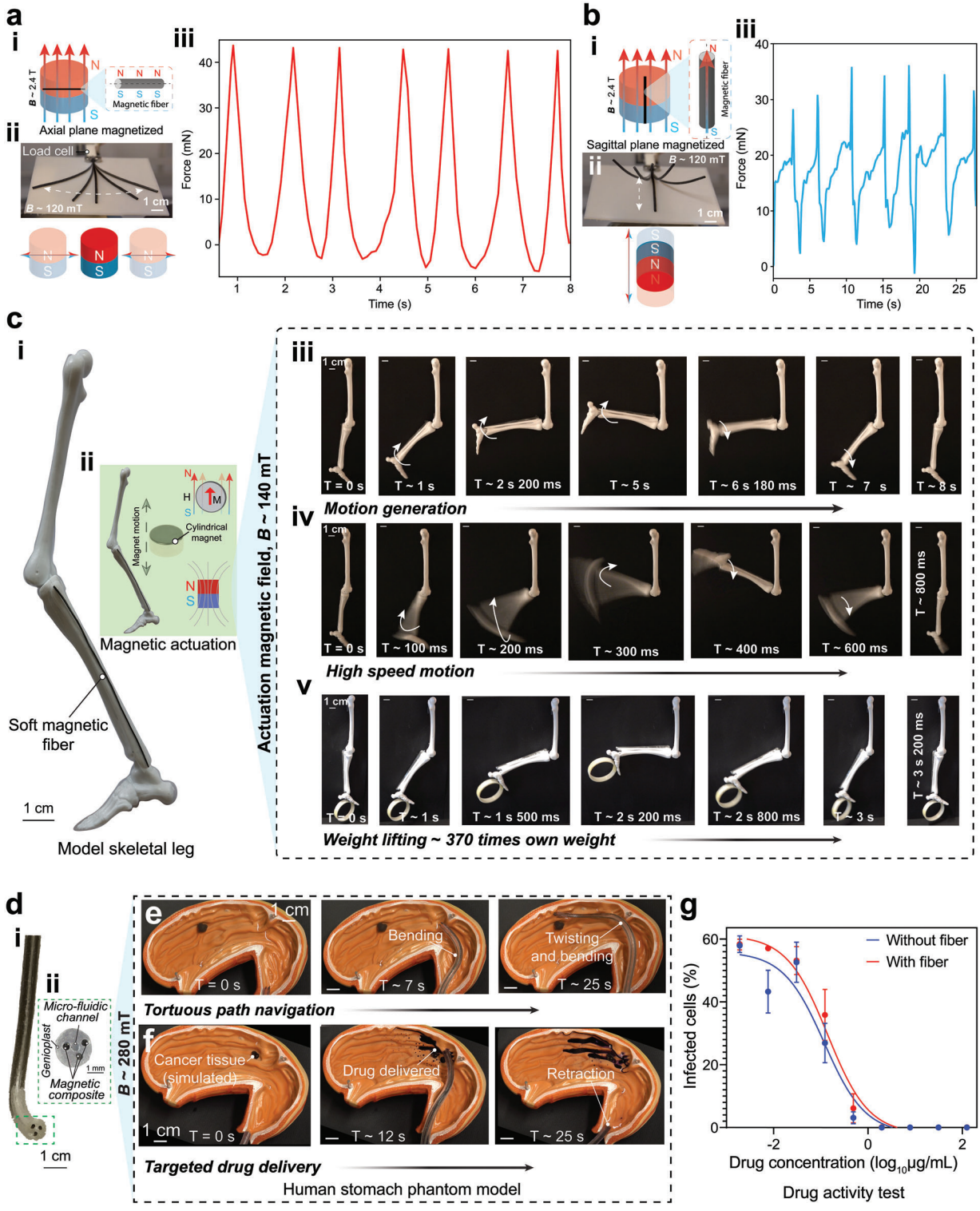

Figure 3. Magnetic fiber domain selection and the motion profile. a,b) Magnetic fiber magnetized in the axial plane (a) and the sagittal plane (b-i); blocking force experiment shown as the generated force applied onto a load cell by magnetic fibers, as well as photographs illustrating the experiment (ii,iii). c) Model skeletal leg with magnetic fiber fastened in the lower part (i), and an external magnetic field actuation orientation profile (ii), different speed motion generation and weight-lifting (iii–v). d) Optical microscopy image of a magnetic fiber (i) integrating three magnetic composites and a hollow core in the center for drug delivery conduit assisting minimally invasive surgery (ii). e) An external magnetic field of 280 mT is used to steer the magnetic fiber for tortuous path navigation inside a human stomach phantom model with the esophagus and simulated diseased tissue. f) A similar magnetic field is used for navigation and drug delivery and eventually retracted from the phantom model. g) 20 cm-long fiber-assisted CD-C11-6'SLN drug delivery on infected MDCK cell population with the H1N1 virus.

have similar responses when we inject drugs via a magnetic fiber-based model catheter, compared to when the drug is injected via conventional methods. This further establishes that the model catheter can be used as a vehicle for drug delivery in practical settings. For prolonged surgical procedures in an aqueous environment, coating with antifouling agents such as biocompatible hydrogel materials can help and also will act as lubrication for navigation purposes.[68,69]

We now move from single fiber configurations to investigating the efficacy of collective effects of magnetic fibers integrated within conformal and stretchable advanced 2D magnetic textiles. Owing to their small diameter yet resilient nature, magnetic fibers are potentially amenable to be integrated within textiles using a variety of techniques such as knitting and weaving at industrial scales.[45,50] Moreover, the ability to magnetize differently several domains along the fiber axis can be exploited to induce innovative textile movement depending on how the fiber is integrated and the orientation of the external magnetic field. As we further demonstrate below, we choose a composite with 20 vol% of the magnetic particle to optimize the interplay between the magnetic force experienced by the textile, and the softness of the fiber that enables greater motion.

We produced fibers with an MRE 20 core and a Genioplast cladding. We mechanically removed the Genioplast cladding after drawing thanks to the weak adhesion between Genioplast and SEBS, achieving fibers with a diameter of 300 μm (**Figure 4**a(i)). To impart the fiber with different magnetization orientations along its axis, we placed the fiber in a mold that oriented the axis differently. Applying a uniform unidirectional magnetic field magnetizes the different domains according to the local orientation of the fiber axis, as shown in Figure 4a(ii,iii). For example, to obtain a sinusoidal deformation upon applying a magnetic field, we positioned the fiber into a mold that imposes a sinusoidal shape to the fiber. An alternating magnetic polarity of the north (N) and south (S) poles is thus distributed over the fiber length after magnetization. The fiber is subsequently weaved into a textile (Figure 4a(iii)) with a prescribed pattern. As shown in Figure 4a(iii), when we weave the fiber in a loop, alternating N and S poles are distributed along the fibers in the textile. Approaching a magnet aligned with the center of symmetry of the textile generates a repulsion/attraction pattern of the N and S domains, leading to a 3D sinusoidal textile shape with an amplitude that depends on the intensity of the applied magnetic field as shown in Figure 4b(i,ii). By applying the magnetic field only close to the side where a single N (or S) dominated pattern is located, the textile shape morphs locally into a dome pattern with varying curvature depending on the external magnetic field strength (Figure 4c(i)). Next, as we move the magnet toward the textile's edge, the dome pattern buckles out of the plane to reach a 3D equilibrium shape to minimize the total strain energy of the continuum structure (Figure 4c(ii)).

This deformation can be rationalized by looking at the constitutive equations that will lead to a mechanical stress in the fiber upon applying an external magnetic field. It is well established[70] that an applied magnetic field will generate a magnetic Cauchy stress $\boldsymbol{\sigma}^{\text{magnetic}} = -\mathbf{B}\otimes\mathbf{FM}$, where we denote the magnetic moment density (or magnetization) inside the ferromagnetic soft material by a vector **M**, and the externally applied magnetic field by a vector **B**. The deformation at any point of the material is characterized by the deformation gradient tensor, **F**. Meanwhile, the deformation of the material generates an elastic Cauchy stress ($\boldsymbol{\sigma}^{\text{elastic}}$), which is also a function of $\boldsymbol{F}$ defined by hyperelastic constitutive models such as the neo-Hookean model.[23] The total Cauchy stress applied to the magnetic textile is then given by $\boldsymbol{\sigma} = \boldsymbol{\sigma}^{\text{magnetic}} + \boldsymbol{\sigma}^{\text{elastic}}$, which dictates the overall magnetic textile's shapemorphing behavior.[70,71]

Next, we investigated the effect of the magnetic particle loading on the textile deformation. As we explained above, there is indeed a trade-off between an increase in magnetic response with higher loading, and a concomitant increase in stiffness that lowers the mechanical response. We experimentally validated the optimal magnetic microparticles' volume fraction to exhibit the highest Cauchy stress, by measuring the angle of curvature θ (deg) (Figure 4c(iii)) of the dome shape for fibers with different particles loading. MRE 20 fibers exhibited the larger deformation hence the maximum Cauchy stress, and we used this level of loading in the remaining investigation of magnetic textiles. When placed on a force-sensitive plate, an MRE 20-based magnetic textile of 6×6 cm^2 surface area weaved from a 10 m long magnetic fiber was measured to generate a force of 22 N when approached by a 250 mT external magnet (Figure 4c(iv)). This level of force is starting to be of interest in rehabilitation purposes and in soft prosthesis to assist movements or attenuate excessive loads. When the external magnetic field is rotating clockwise or counterclockwise the magnetic textile follows and rolls over to fold and unfold accordingly (Figure 4d(i,ii)), a motion that could be used for transporting cargo, for example.

Another example of an interesting shape-morphing behavior from a textile is presented in **Figure 5**a. We weaved a 5 m long magnetic fiber into a textile of 4×4 cm^2 surface area, that we subsequently magnetized with a magnetic orientation perpendicular to the textile plane (Figure 5a(i)). A cylindrical permanent magnet of 250 mT peak magnetic field was then brought near and away from the textile following a cyclic behavior shown in Figure 5a(ii). One end of the magnetic textile was fixed onto a 3D-printed thin polycarbonate (PC) surface to restrict the motion to one degree of freedom. We could then observe the magnetic textile's flapping motion following reliably the trapezoidal magnetic field actuation profile as depicted in Figure 5a(ii) (Stage 1–8).

To demonstrate the resilience of the magnetic fibers and associated textiles, we tested them under a heavy impact load, as well as in a washing machine. We anticipated that soft systems could absorb a large deformation force given the nature of the elastomeric materials we used.[72] We hence subjected a magnetic textile to be run over by a car, which was equivalent to a 330 kg of weight on the textiles, for six consecutive times (Figure 5b(i); Movie S4, Supporting Information). We measured the magnetic properties of the textile before and after the heavy mechanical constraint via measuring the force applied by the textile when on a load cell and actuated by a magnet. We observed a 2.3% change over several cycles in the peak force of 162.4 mN before and after the impact test demonstrating the strong resilience of the magnetic textile (Figure 5b(ii)).

To address the requirement of some functional textiles to sustain several washing and drying cycles, we performed a machine-washing test (Figure 5c(i)). Magnetic textiles underwent 6 wash cycles of 15 min each, with a few drops of liquid detergent

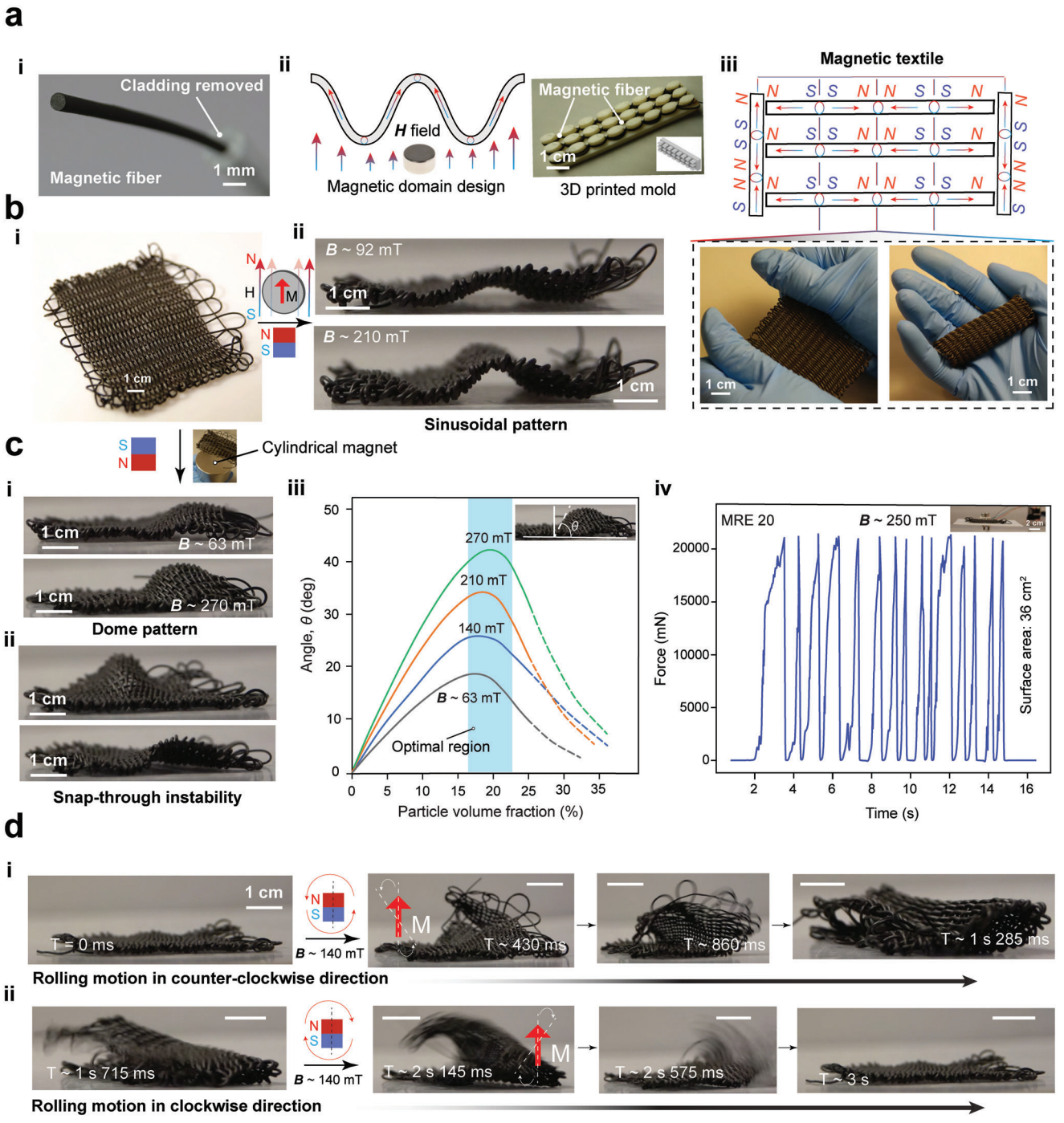

Figure 4. Magnetic textile fabrication and shape morphing. a) Photograph of a magnetic fiber while cladding material is removed (i), fibers are accommodated into a 3D printed mold and magnetized in a sinusoidal pattern (ii), finally magnetized fibers are weaved to form a magnetic textile with a sinusoidal magnetic domain engineered inside (iii). b) 2D magnetic textile (i) shape morphs into a 3D sinusoidal architecture (ii). c) Magnetic textile shape morphs into dome pattern (i), buckles down depicting snap-through instability (ii), curvature (θ) changes with ferromagnetic particles volume fraction (iii), and blocking force calculation from the load cell (iv). d) External magnetic field rotates in a clockwise and counter-clockwise direction while the magnetic fibers roll and unroll accordingly (i,ii).

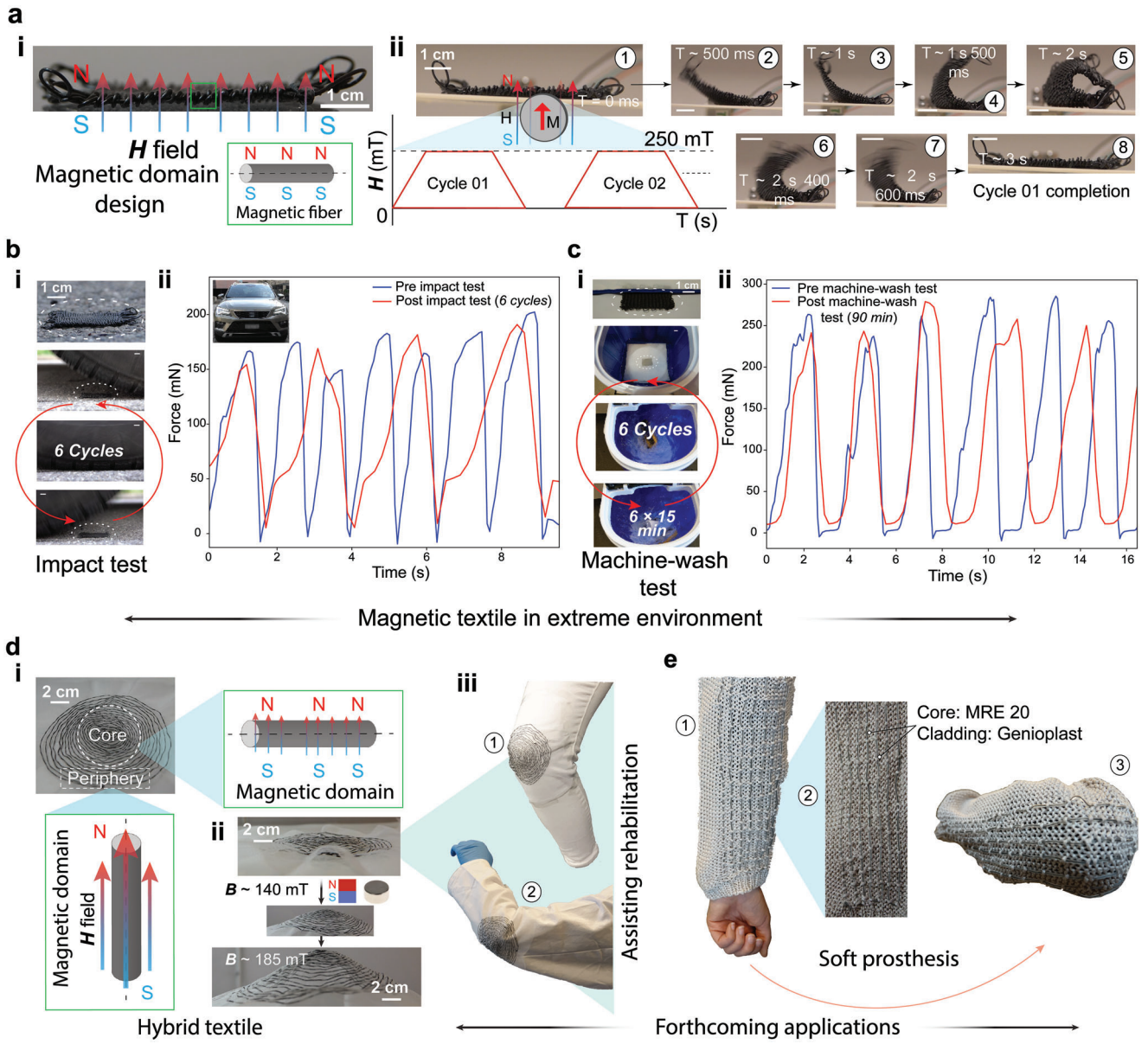

Figure 5. Magnetic textiles in extreme environments and forthcoming applications. a) Magnetic textile and their magnetization profile (i), flapping motion during external magnetic field actuation (Stage 1–8) (ii). b,c) Magnetic textiles and their performance in extreme environments such as running over by a car (b-i,ii), and machine-wash test and washability of the magnetic textiles (c-i,ii). d) Magnetic fibers warping concentric circles with different magnetic domains into a dense weft gauge swab to form hybrid textile (i), and tether-free actuation to form a dome shape with varying curvature (ii) for assisting rehabilitation (Stage 1–2) (iii). e) Magnetic fibers integrated into a piece of fabric demonstrating near-term multilayer, integrated smart textiles for soft prosthesis (Stage 1–3).

added to the water (Movie S5, Supporting Information). We could measure ≈2% change in the recorded force of 258 mN before and after the machine-wash test as depicted in Figure 5c(ii). These results further reinforce the potential of magnetic textiles to be used as medical systems thanks to their high reliability and inherent mechanical compliance and robustness in practical settings. Additionally, medical grade SEBS samples and SEBS composites are biocompatible,[73] support MTT assay, and can be employed to grow C2C12 cells,[74] and to use as transdermal patches.[75]

Finally, to propose a perspective of applications of such magnetic textiles, we integrated magnetic fibers into a fabric with a concentric circles configuration (Figure 5d(i)). One example of functionalization could be to use this type of system in a rehabilitation setting where the textiles would sense and mechanically compensate an excessive pressure on an injured joint. For this, the periphery magnetic fibers were magnetized in the sagittal plane while the core concentric magnetic fibers are magnetized in an axial plane direction. Inside the hybrid textile, the edge

attracts the external magnetic field while the core repels hence a dome shape is produced (Figure 5d(ii)). Increasing external magnetic field strength from 140 to 185 mT in turn increases the dome shape curvature as depicted in Figure 5d(ii).

3. Conclusion

We have demonstrated soft thermally drawn multimaterial magnetic fibers and functional textiles for tether-free actuation. We developed polymeric magnetic fibers with an extreme aspect ratio of 10^5 and diameters as low as 300 µm, that integrate elastomeric composites with ferromagnetic microparticles. Via an in-depth analysis of the rheological and mechanical properties, and looking in detail at the filler distribution via computed tomography, we could identify the right filler composition and polymeric matrix for optimum performance. We demonstrated the magnetic actuation of the fibers both to trigger movement but also to apply a force and lift an object several orders of magnitudes heavier than the fiber's own weight. We exploited the versatility of the thermal drawing process to realize fibers with complex architectures including several magnetic domains and microfluidic channels. Complex fiber architectures enable to perform advanced movement paths and actuation, while allowing for multiple functionalities. Given the soft mechanical properties, the magnetic fibers are well amenable to be integrated within textiles using different textile processes. We weaved fibers into fabrics and by magnetizing locally with different orientations along the fiber axis, and controlling the positioning of the fiber in the fabric, we could demonstrate advanced textile deformation and shape morphing. We envision that similar strategies can be applied to realize medical textiles that will be of precious help to patients in rehabilitation, providing on-demand support for damaged joints. In Figure 5d(iii),e, we show examples of magnetic fibers wrapped within fabrics of different configurations for potential applications in soft prosthesis. The ability of textile integration paves the way toward novel soft prosthesis and advanced fabrics with innovative magnetic properties. Advanced soft magnetic fibers and textiles can offer novel opportunities for soft prosthesis but also surgical tools, wearable robotics and rehabilitation, the internet of things, as well as human-machine interactions.

4. Experimental Section

Base Materials: p-Xylene (Chemie Brunschwig; ≥ 99%), isopropanol (Sigma-Aldrich; ≥ 99%), toluene (Sigma-Aldrich; ≥ 99%), and chloroform (Sigma-Aldrich; ≥ 99%) were used as received without additional modification. SEBS (Kraton), SIS (Kraton), and Genioplast (Wacker) were used as the TPE materials in their pristine form. NdFeCoB alloy-based magnetic microparticles (MQFP-B+(D50 = 5 µm)-10215-089; Magnequench) of a diameter of 2–5 µm were used, with a Curie temperature of 360 °C according to the supplier. A universal mold release (Smooth-On) was used to decouple the internal structure from the metallic molds. A Milli-Q water purifier was used to wash the polymer pellets throughout and clean the associated powder component.

Fabrication of Magnetic Fibers: The fabrication of the preform was initiated with standard TPE processing techniques, including the shaping of individual material parts by compression molding or mechanical machining, and the subsequent assembly of the parts and consolidation as a final compression molding step. The rectangular, circular, and triangular preforms with predefined geometries were fabricated using custom-made steel molds with desired outer shape and interior mold core. TPE granules were filled inside the custom-made steel mold and compress-molded at ≈0.9 bar, 180 °C for 12 h. For producing magnetic composites, SEBS granules were added to p-xylene to reach a concentration of 2 wt.%, while SIS and Genioplast granules were dissolved inside isoprop/toluol mixture (2:1) for attaining a concentration of 2.5 wt.%. Magnetic microparticles of different volume concentrations were then added into SEBS, Genioplast, and SIS solution and the magnetic stirring process was used for 24 h to avoid any agglomeration. Poly(tetrafluoroethylene) (PTFE)/polypropylene stain-and stick-resistant plastic pan (McMaster-Carr) was then used to drop cast the magnetic composite and wait for 12 h for solvent evaporation to form the thin magnetic composite layer.

The magnetic composite's thin film was then cut into small pieces and placed inside the cylindrical steel mold housed with temperature-resistant PTFE hollow core tubes (6 mm inner diameter, McMaster-Carr) for compression molding in a consolidation oven at ≈0.9 bar, 180 °C for 12 h. Next, the magnetic composite columns were de-molded and pushed gently inside a cylindrical and triangular preform. For hollow core preforms, aluminum bars (4-6 mm in diameter, Thorlabs) covered with Teflon tape were used during the consolidation and compression molding step and subsequently removed to obtain the desired cavity. Rectangular preforms were fabricated by stacking TPE and magnetic composite films of pre-defined thickness and compression-molded at 0.1 bar, 140 °C for 20 min using a Meyer press (Maschinenfabrik Herbert Meyer GmbH APV-2525/16).

Next, the preforms were placed into a three-zone vertical tube furnace of a custom-built draw tower. SEBS, Genioplast, and SIS fibers were thermally drawn keeping the top and bottom-zone temperatures at 90 and 70 °C respectively, while changing the middle-zone temperature of 200 °C for SEBS, 240 °C for Genioplast, and 220 °C for SIS. The setting temperature for the top, middle, and bottom zone to manufacture magnetic fibers were 100, 265, and 70 °C, respectively. The preform was then fed into the furnace at a speed of 1 mm min^{-1} and take-up speeds ranging from 100 to 900 mm min^{-1}, resulting in diameter scale-down ratios of 10 to 30. In fiber post-processing, the fibers were first cut into suitable lengths segments, and supporting Genioplast layers were removed to initiate magnetic fiber-based characterization.

Materials Characterization: The core and cladding material of the magnetic fibers, that is MRE, SEBS, Geniomer, and SIS were characterized for their rheological, magnetic, and mechanical properties. Disks of diameter 25 mm and thickness of 1 mm were fabricated by compression molding (custom press, Lauffer), and was analyzed by oscillatory shear rheology (AR 2000, TA Instruments), where the temperature was increased from 50 to 250 °C at a ramp speed of 3 °C min^{-1} under the oscillatory shear strain of frequency 1 Hz and amplitude 1%. The frequency sweep experiments were performed from 10^0 to 10^{-4} Hz at a temperature of 160 °C and a strain amplitude of 0.1%. For dynamic oscillation stress sweeps, the stress amplitude was increased from 10^1 to 10^4 Pa at a temperature of 160 °C at a fixed angular frequency of 1 rad s^{-1}.

The fibers were placed inside 3D-printed molds and rotated differently to impart different magnetization orientations along its axis. Next, the non-magnetized fibers were separately magnetized using an applied uniaxial magnetic field (≈2.4 T, perpendicular to the equatorial plane) generated by an impulse magnetizer (IM-K-010020-A, Magnet-Physik Dr. Steingroever GmbH). The magnetizing coil diameter and height were both of 12 cm. To assess the quality of magnetic particles alignment by measuring the magnetic moment density and magnetization of the 10–25 vol% NdFeCoB-SEBS fibers, a vibrating sample magnetometer (VSM) test (Quantum Design PPMS, DynaCoolTM) was used. The magnetic hysteresis loops for 10–25 vol% NdFeCoB-SEBS fibers were measured between −2.5 and +2.5 T.

Corresponding composite densities of the 10, 15, 20, and 25 vol% NdFeCoB-SEBS were measured using a pycnometer to be 1.431, 1.762, 2.395, and 2.5 g cm^{-3}, respectively considering the NdFeCoB particle's density as 7.61±0.20 g cm^{-3} as reported by the supplier. Cylindrical NdFeB magnets S-70-35-N (70 mm diameter and 35 mm thickness; Supermagnete), S-60-05-N (60 mm diameter and 5 mm thickness; Supermagnete) were used for shape morphing and magnetic fiber steering operations. For all the magnetic field-related calculations, the uniaxial field direction

AC/DC magnetic meter model: PCE-MFM 3000 (PCE Instruments) was used.

Mechanical properties of the thermally drawn fibers were quantified under standard tensile testing (Z005 with 50 N low cell, Zwick/Roell), using fiber samples of diameter 1.5 mm and clamped length 30 mm, and at a speed of 500 and 50 mm min^{-1}. All the experiments in this paper unless specified otherwise were performed at least three-five times ($n = 3–5$) and data were presented as mean with freshly prepared magnetic fiber samples and textiles.

Imaging and Videography: SEM was performed on a Zeiss GeminiSEM 300 with an acceleration voltage of 3 kV using the In-Lens and the Everhart–Thornley detector. The magnetic fibers were at first immersed in liquid nitrogen for several minutes, and soon after were cut at room temperature. Next, the fiber samples were coated with a 10 nm Au film with a platinum/iridium/gold sputter coater (Quorum) and loaded inside the SEM stub. The fabricated fibers were also assessed using optical microscopy (DM 2700 M, Leica). The magnetic fiber's motion profile, textile's shape-morphing, and performance in extreme conditions, navigation, and drug delivery experiments were recorded by a camera (RX100, Canon). Magnetic textile's curvature measurement with varying magnetic microparticles concentration was analyzed using computer vision (OpenCV in Python), where from the coordinates of the base and the tip of dome-shaped textiles were extracted.

X-ray Microtomography: Ultratom from RX-Solutions was used for the X-ray microtomography whereas for the scan the nanotube was used. For the magnetic composite at the preform stage voxel size of 1.2 µm, a voltage of 80 kV, a current of 67 µA, an aluminum filter of 0.1 mm, 1632 projections while a frame rate of 3 images per second, and an average frame of 13 images were used. For the magnetic fibers, a voxel size of 0.9 µm, a voltage of 80 kV, a current of 69 µA, and a copper filter of 0.2 mm, 1632 projections, a frame rate of 3 images per second, and an average frame of 15 images were used.

Force Sensing: The blocking force generated by thermally drawn magnetic fibers with different magnetic domains and dimensions of 5 cm in length and ≈1200 µm diameter was compared. Magnetic textiles of different surface areas were used for force-sensing experiments. The experimental setup consisted of a 500 g load cell made of a straight aluminum bar (TAL221, SparkFun) equipped with a 3D printed PC platform (8×8 cm^2) of 1 mm thickness onto which the magnetic fibers and magnetic textiles were pressed. The data was collected using an amplifier (HX711, SparkFun) coupled to a microcontroller (Arduino Uno, Arduino).

Cells and Viruses: MDCK cells were plated at 3×10^5 cells per well in 24-well plates and incubated at 37 °C for 24 h in Dulbecco's modified Eagle medium (DMEM) Glutamax with 5% fetal bovine serum (FBS). Serial dilution of CD-C11-6'SLN drug was performed in a medium and the drug was used to treat the H1N1 virus using a syringe and 20 cm long fiber. The drug and viruses were incubated for 1 h at 37 °C and then the MDCK cells were infected. Next, the infected cells were incubated for 24 h and the cells were then fixed and permeabilized with 100% cold methanol for 20 min at −20 °C. Subsequently, the cells were stained with a mouse primary antibody against influenza and a secondary antibody anti-mouse Alexa Fluor 488. Finally, the nucleus of the total cells was stained with 4′,6-diamidino-2-phenylindole (DAPI).

Mechanical and Machine-Wash Tests: A closely designed running track was used and the magnetic textile was then placed to test the textile's mechanical resilience by running over with a 2020 SEAT Ateca car for six consecutive times. For the machine-wash test, the magnetic textile was placed inside a water-permeable protective laundry bag and a portable mini-washing machine (PUCWM11, PYLE) was used. The magnetic textile experienced 6 machine cycles of 15 min each that was 90 min of total washing time on "cotton" wash mode was employed at room temperature. A few drops of liquid detergent were used during machine washing.

Supporting Information

Supporting Information is available from the Wiley Online Library or from the author.

Acknowledgements

The authors thank Prof. Pedro M. Reis, Prof. Francesco Stellacci, Dr. Dong Yan, Dr. Yong Liu, Gary Perrenoud, Pierre-Luc Piveteau, Arefeh Abbasi, Jigyasa Nigam, Dr. Shahrzad Shadman, Dr. Bastien Schyrr, Dr. Inès Richard, Yan Meng, and Laurène Tribolet for conducive discussion and experimental support. The authors also thank the Laboratory for Processing of Advanced Composites (LPAC) at EPFL for the support in terms of equipment usage. F.S. acknowledges the support of the European Research Council (ERC Starting Grant 679211 "FLOWTONICS") and the Swiss National Science Foundation (SNSF Grant 204579 "Highly integrated soft fibers for advanced sensing and actuation").

Open access funding provided by Ecole Polytechnique Federale de Lausanne.

Conflict of Interest

The authors declare no conflict of interest.

Data Availability Statement

The data that support the findings of this study are available from the corresponding author upon reasonable request.

Keywords

magnetic polymer composites, multimaterial fibers, smart textiles, soft actuators, soft materials

Received: December 28, 2022
Revised: March 17, 2023
Published online:

[1] J. A. Rogers, *Science (80-.)*. **2013**, *341*, 968.
[2] J. A. Rogers, T. Someya, Y. Huang, *Science (80-.)*. **2010**, *327*, 1603.
[3] D. H. Kim, N. Lu, R. Ma, Y. S. Kim, R. H. Kim, S. Wang, J. Wu, S. M. Won, H. Tao, A. Islam, K. J. Yu, T. Il Kim, R. Chowdhury, M. Ying, L. Xu, M. Li, H. J. Chung, H. Keum, M. McCormick, P. Liu, Y. W. Zhang, F. G. Omenetto, Y. Huang, T. Coleman, J. A. Rogers, *Science (80-.)*. **2011**, *333*, 838.
[4] D. J. Lipomi, M. Vosgueritchian, B. C. K. Tee, S. L. Hellstrom, J. A. Lee, C. H. Fox, Z. Bao, *Nat. Nanotechnol.* **2011**, *6*, 788.
[5] S. C. B. Mannsfeld, B. C. K. Tee, R. M. Stoltenberg, C. V. H. H. Chen, S. Barman, B. V. O. Muir, A. N. Sokolov, C. Reese, Z. Bao, *Nat. Mater.* **2010**, *9*, 859.
[6] G. Schwartz, B. C. K. Tee, J. Mei, A. L. Appleton, D. H. Kim, H. Wang, Z. Bao, *Nat. Commun.* **2013**, *4*, 1859.
[7] T. Chen, O. R. Bilal, K. Shea, C. Daraio, *Proc. Natl. Acad. Sci. USA* **2018**, *115*, 5698.
[8] A. Kotikian, R. L. Truby, J. W. Boley, T. J. White, J. A. Lewis, *Adv. Mater.* **2018**, *30*, 1706164.
[9] M. Kanik, S. Orguc, G. Varnavides, J. Kim, *Science (80-.)*. **2019**, *150*, 145.
[10] M. Rogóż, H. Zeng, C. Xuan, D. S. Wiersma, P. Wasylczyk, *Adv. Opt. Mater.* **2016**, *4*, 1689.
[11] H. Shahsavan, A. Aghakhani, H. Zeng, Y. Guo, Z. S. Davidson, A. Priimagi, M. Sitti, *Proc. Natl. Acad. Sci. USA* **2020**, *117*, 5125.
[12] A. Aghakhani, O. Yasa, P. Wrede, M. Sitti, *Proc. Natl. Acad. Sci. USA* **2020**, *117*, 3469.
[13] M. Kaynak, P. Dirix, M. S. Sakar, *Adv. Sci.* **2020**, *7*, 2001120.

[14] M. Wehner, R. L. Truby, D. J. Fitzgerald, B. Mosadegh, G. M. Whitesides, J. A. Lewis, R. J. Wood, *Nature* **2016**, *536*, 451.
[15] C. A. Aubin, S. Choudhury, R. Jerch, L. A. Archer, J. H. Pikul, R. F. Shepherd, *Nature* **2019**, *571*, 51.
[16] Y. Kim, H. Yuk, R. Zhao, S. A. Chester, X. Zhao, *Nature* **2018**, *558*, 274.
[17] Y. Kim, E. Genevriere, P. Harker, J. Choe, M. Balicki, R. W. Regenhardt, J. E. Vranic, A. A. Dmytriw, A. B. Patel, X. Zhao, *Sci. Rob.* **2022**, *7*, eabg9907.
[18] Y. Kim, G. A. Parada, S. Liu, X. Zhao, *Sci. Rob.* **2019**, *4*, eaax7329.
[19] M. Sitti, D. S. Wiersma, *Adv. Mater.* **2020**, *32*, 1906766.
[20] M. Li, A. Pal, A. Aghakhani, A. Pena-Francesch, M. Sitti, *Nat. Rev. Mater.* **2022**, *7*, 235.
[21] L. Hines, K. Petersen, G. Z. Lum, M. Sitti, *Adv. Mater.* **2017**, *29*, 1603483.
[22] S. I. Rich, R. J. Wood, C. Majidi, *Nat. Electron.* **2018**, *1*, 102.
[23] Y. Kim, X. Zhao, *Chem. Rev.* **2022**, *122*, 5317.
[24] S. Wu, W. Hu, Q. Ze, M. Sitti, R. Zhao, *Multifunct. Mater.* **2020**, *3*, 042003.
[25] Y. Tang, M. Li, T. Wang, X. Dong, W. Hu, M. Sitti, *Adv. Mater.* **2022**, *34*, 2204185.
[26] V. M. Kadiri, C. Bussi, A. W. Holle, K. Son, H. Kwon, G. Schütz, M. G. Gutierrez, P. Fischer, *Adv. Mater.* **2020**, *32*, 2001114.
[27] C. Peters, M. Hoop, S. Pané, B. J. Nelson, C. Hierold, *Adv. Mater.* **2016**, *28*, 533.
[28] X. Kuang, S. Wu, Q. Ze, L. Yue, Y. Jin, S. M. Montgomery, F. Yang, H. J. Qi, R. Zhao, *Adv. Mater.* **2021**, *33*, 2102113.
[29] Q. Ze, X. Kuang, S. Wu, J. Wong, S. M. Montgomery, R. Zhang, J. M. Kovitz, F. Yang, H. J. Qi, R. Zhao, *Adv. Mater.* **2020**, *32*, 2070025.
[30] Z. Ren, W. Hu, X. Dong, M. Sitti, *Nat. Commun.* **2019**, *10*, 2703.
[31] E. B. Joyee, Y. Pan, *Soft Rob.* **2019**, *6*, 333.
[32] C. Zhou, Y. Yang, J. Wang, Q. Wu, Z. Gu, Y. Zhou, X. Liu, Y. Yang, H. Tang, Q. Ling, L. Wang, J. Zang, *Nat. Commun.* **2021**, *12*, 5072.
[33] Z. Yang, L. Zhang, *Adv. Intell. Syst.* **2020**, *2*, 2000082.
[34] C. Chautems, A. Tonazzini, Q. Boehler, S. H. Jeong, D. Floreano, B. J. Nelson, *Adv. Intell. Syst.* **2020**, *2*, 1900086.
[35] N. K. Persson, J. G. Martinez, Y. Zhong, A. Maziz, E. W. H. Jager, *Adv. Mater. Technol.* **2018**, *3*, 1700397.
[36] T. Xu, J. Zhang, M. Salehizadeh, O. Onaizah, E. Diller, *Sci. Rob.* **2019**, *4*, eaav4494.
[37] W. Hu, G. Z. Lum, M. Mastrangeli, M. Sitti, *Nature* **2018**, *554*, 81.
[38] J. Zhang, Z. Ren, W. Hu, R. H. Soon, I. C. Yasa, Z. Liu, M. Sitti, *Sci. Rob.* **2021**, *6*, eabf0112.
[39] J. Kim, S. E. Chung, S. E. Choi, H. Lee, J. Kim, S. Kwon, *Nat. Mater.* **2011**, *10*, 747.
[40] J. Cui, T. Y. Huang, Z. Luo, P. Testa, H. Gu, X. Z. Chen, B. J. Nelson, L. J. Heyderman, *Nature* **2019**, *575*, 164.
[41] H. W. Huang, M. S. Sakar, A. J. Petruska, S. Pané, B. J. Nelson, *Nat. Commun.* **2016**, *7*, 12263.
[42] H. W. Huang, T. Y. Huang, M. Charilaou, S. Lyttle, Q. Zhang, S. Pané, B. J. Nelson, *Adv. Funct. Mater.* **2018**, *28*, 1802110.
[43] J. Liu, Z. Du, Q. Wang, B. Su, Z. Xia, *ACS Appl. Mater. Interfaces* **2022**, *14*, 2113.
[44] R. Wang, Z. Du, Z. Xia, J. Liu, P. Li, Z. Wu, Y. Yue, Y. Xiang, J. Meng, D. Liu, W. Xu, X. Tao, G. Tao, B. Su, *Adv. Funct. Mater.* **2022**, *32*, 2107682.
[45] G. Loke, W. Yan, T. Khudiyev, G. Noel, Y. Fink, *Adv. Mater.* **2020**, *32*, 1904911.
[46] J. Xiong, J. Chen, P. S. Lee, *Adv. Mater.* **2021**, *33*, 2002640.
[47] M. Chen, Z. Wang, K. Li, X. Wang, L. Wei, *Adv. Fiber Mater.* **2021**, *3*, 1.
[48] A. Leber, C. Dong, S. Laperrousaz, H. Banerjee, M. E. M. K. Abdelaziz, N. Bartolomei, B. Schyrr, B. Temelkuran, F. Sorin, *Adv. Sci.* **2023**, *10*, 2204016.
[49] C. Dong, A. Leber, T. Das Gupta, R. Chandran, M. Volpi, Y. Qu, T. Nguyen-Dang, N. Bartolomei, W. Yan, F. Sorin, *Nat. Commun.* **2020**, *11*, 3537.
[50] W. Yan, A. Page, T. Nguyen-Dang, Y. Qu, F. Sordo, L. Wei, F. Sorin, *Adv. Mater.* **2019**, *31*, 1802348.
[51] W. Yan, C. Dong, Y. Xiang, S. Jiang, A. Leber, G. Loke, W. Xu, C. Hou, S. Zhou, M. Chen, R. Hu, P. P. Shum, L. Wei, X. Jia, F. Sorin, X. Tao, G. Tao, *Mater. Today* **2020**, *35*, 168.
[52] F. Sordo, E. R. Janecek, Y. Qu, V. Michaud, F. Stellacci, J. Engmann, T. J. Wooster, F. Sorin, *Adv. Mater.* **2019**, *31*, 1807282.
[53] M. A. Schmidt, A. Argyros, F. Sorin, *Adv. Opt. Mater.* **2016**, *4*, 13.
[54] M. Bayindir, F. Sorin, A. F. Abouraddy, J. Viens, S. D. Hart, J. D. Joannopoulos, Y. Fink, *Nature* **2004**, *431*, 826.
[55] M. Bayindir, Y. Abouraddy, AF Sorin, F. John, D. Joannopoulos, Fink, *Opt. Photonics News* **2004**, *15*, 24.
[56] S. Shadman, T. Nguyen-Dang, T. Das Gupta, A. G. Page, I. Richard, A. Leber, J. Ruza, G. Krishnamani, F. Sorin, *Adv. Funct. Mater.* **2020**, *30*, 1910283.
[57] Y. Qu, T. Nguyen-Dang, A. G. Page, W. Yan, T. Das Gupta, G. M. Rotaru, R. M. Rossi, V. D. Favrod, N. Bartolomei, F. Sorin, *Adv. Mater.* **2018**, *30*, 1707251.
[58] A. Leber, A. G. Page, D. Yan, Y. Qu, S. Shadman, P. Reis, F. Sorin, *Adv. Funct. Mater.* **2020**, *30*, 1904274.
[59] A. Leber, C. Dong, R. Chandran, T. Das Gupta, N. Bartolomei, F. Sorin, *Nat. Electron.* **2020**, *3*, 316.
[60] C. Dong, A. Leber, D. Yan, H. Banerjee, S. Laperrousaz, T. Das Gupta, S. Shadman, P. M. Reis, F. Sorin, *Sci. Adv.* **2022**, *8*, 869.
[61] T. Nguyen-Dang, A. C. de Luca, W. Yan, Y. Qu, A. G. Page, M. Volpi, T. Das Gupta, S. P. Lacour, F. Sorin, *Adv. Funct. Mater.* **2017**, *27*, 1605935.
[62] J. G. Drobny, *Handbook of Thermoplastic Elastomers*, 2nd Ed., Elsevier **2014**.
[63] S. Park, K. Mondal, R. M. Treadway, V. Kumar, S. Ma, J. D. Holbery, M. D. Dickey, *ACS Appl. Mater. Interfaces* **2018**, *10*, 11261.
[64] L. Wang, Y. Chen, L. Lin, H. Wang, X. Huang, H. Xue, J. Gao, *Chem. Eng. J.* **2019**, *362*, 89.
[65] C. R. Siviour, J. L. Jordan, *J. Dyn. Behav. Mater.* **2016**, *2*, 15.
[66] J. Diani, B. Fayolle, P. Gilormini, *Eur. Polym. J.* **2009**, *45*, 601.
[67] Y. Kraftmakher, *Eur. J. Phys.* **2007**, *28*, 409.
[68] J. Yang, B. Xue, Y. Zhou, M. Qin, W. Wang, Y. Cao, *Adv. Mater. Technol.* **2021**, *6*, 2000911.
[69] D. Su, X. Bai, X. He, *Eur. Polym. J.* **2022**, *181*, 111665.
[70] R. Zhao, Y. Kim, S. A. Chester, P. Sharma, X. Zhao, *J. Mech. Phys. Solids* **2019**, *124*, 244.
[71] A. Dorfmann, R. W. Ogden, *Eur. J. Mech., A: Solids* **2003**, *22*, 497.
[72] R. V. Martinez, A. C. Glavan, C. Keplinger, A. I. Oyetibo, G. M. Whitesides, *Adv. Funct. Mater.* **2014**, *24*, 3003.
[73] J. Hou, Q. Shi, W. Ye, Q. Fan, H. Shi, S. C. Wong, X. Xu, J. Yin, *ACS Appl. Mater. Interfaces* **2014**, *6*, 20868.
[74] S. Ribeiro, P. Costa, C. Ribeiro, V. Sencadas, G. Botelho, S. Lanceros-Méndez, *Composites, Part B* **2014**, *67*, 30.
[75] C. G. M. Gennari, G. M. G. Quaroni, C. Creton, P. Minghetti, F. Cilurzo, *Int. J. Pharm.* **2020**, *575*, 118975.